ADVANCED MATERIALS
www.advmat.de

Atomic-Scale Core/Shell Structure Engineering Induces Precise Tensile Strain to Boost Hydrogen Evolution Catalysis

Han Zhu, Guohua Gao, Mingliang Du, Jinhui Zhou, Kai Wang, Wenbo Wu,* Xu Chen, Yong Li, Piming Ma, Weifu Dong, Fang Duan, Mingqing Chen, Guangming Wu, Jiandong Wu, Haitao Yang, and Shaojun Guo**

Tuning surface strain is a new strategy for boosting catalytic activity to achieve sustainable energy supplies; however, correlating the surface strain with catalytic performance is scarce because such mechanistic studies strongly require the capability of tailoring surface strain on catalysts as precisely as possible. Herein, a conceptual strategy of precisely tuning tensile surface strain on Co_9S_8/MoS_2 core/shell nanocrystals for boosting the hydrogen evolution reaction (HER) activity by controlling the MoS_2 shell numbers is demonstrated. It is found that the tensile surface strain of Co_9S_8/MoS_2 core/shell nanocrystals can be precisely tuned from 3.5% to 0% by changing the MoS_2 shell layer from 5L to 1L, in which the strained Co_9S_8/1L MoS_2 (3.5%) exhibits the best HER performance with an overpotential of only 97 mV (10 mA cm^{-2}) and a Tafel slope of 71 mV dec^{-1}. The density functional theory calculation reveals that the Co_9S_8/1L MoS_2 core/shell nanostructure yields the lowest hydrogen adsorption energy (ΔE_H) of −1.03 eV and transition state energy barrier (ΔE_{2H^*}) of 0.29 eV (MoS_2, ΔE_H = −0.86 eV and ΔE_{2H^*} = 0.49 eV), which are the key in boosting HER activity by stabilizing the HER intermediate, seizing H ions, and releasing H_2 gas.

Pursuing renewable and clean hydrogen energy is one of the promising ways in solving the environmental issues and reducing our reliance on fossil fuels.[1–3] The scalable production of hydrogen through electrochemical water splitting requires highly efficient and robust electrocatalysts.[4–6] Developing highly active earth-abundant electrocatalysts for hydrogen evolution reaction (HER) is of far-reaching significance, and recent works have focused on designing and engineering non-noble metal catalysts by maximizing the active sites, integrating with conducting substrate, and tuning the phase and electronic structures to reduce the Gibbs free energy for hydrogen atoms adsorption in order to replace the state-of-the-art platinum-group catalysts.[7–9] The reported hydrogen evolution mechanism of non-noble metal catalysts usually

Dr. H. Zhu, Prof. M. Du, Prof. P. Ma, Prof. W. Dong, Dr. F. Duan, Prof. M. Chen
Key Laboratory of Synthetic and Biological Colloids
Ministry of Education
School of Chemical and Material Engineering
Jiangnan University
Wuxi 214122, China
E-mail: du@jiangnan.edu.cn

Dr. G. Gao, Prof. G. Wu
Shanghai Key Laboratory of Special Artificial Microstructure
School of Physics Science and Engineering
Tongji University
Shanghai 200092, China

Dr. J. Zhou, Dr. K. Wang, Prof. S. Guo
Department of Materials Science & Engineering and BIC-ESAT
College of Engineering
Peking University
Beijing 100871, China
E-mail: guosj@pku.edu.cn

The ORCID identification number(s) for the author(s) of this article can be found under https://doi.org/10.1002/adma.201707301.

[+]Present address: Department of Chemical and Biomolecular Engineering, National University of Singapore, Singapore 117585, Singapore

Dr. W. Wu,[+] Dr. H. Yang
School of Materials Science and Engineering
Zhengzhou University
Zhengzhou 450001, China
E-mail: msewuw@nus.edu.sg

Dr. X. Chen
State Key Laboratory of Chemical Resource Engineering
Beijing University of Chemical Technology
Beijing 100029, China

Dr. Y. Li
Institute of Applied and Physical Chemistry and Center for Environmental Research and Sustainable Technology
Universität Bremen
28359 Bremen, Germany

Dr. J. Wu
School of Material Science and Engineering
North Minzu University
Yinchuan 750021, China

DOI: 10.1002/adma.201707301

involves three steps, including hydrogen atom adsorbed on the catalyst surface, hydrogen molecule formation, and hydrogen molecule desorption from the catalyst surface.[10] The hydrogen adsorption energy (ΔE_H) determines the capability of catalyst to bond the hydrogen atoms,[11] the most key step in impacting HER in the reported non-noble metal catalysts. However, the researchers usually ignore the formation and desorption of hydrogen molecule processes on the catalyst surfaces, which are also important factors for overall efficiency of HER. In particular, there is a transition state (2H*) between the adsorbed hydrogen atoms and formation of hydrogen molecules on catalyst surfaces, and the energy barrier of transition state (ΔE_{2H*}) actually determines the formation and desorption of hydrogen molecules.[12–14]

As is known, not all the atoms in catalysts are catalytically active, restricting the atomic-level structural elucidation and mechanistic understanding of the intrinsically active center.[15] Understanding the structure–performance relationship of multicomponent nanocrystals is very essential for tuning the activity and efficiency, and further facilitating the rational structural design of more efficient electrocatalysts. For the Pt-based bimetallic catalytic systems, structure-relevant strain effect can be used to tune the catalytic reactivity.[16–18] Traditionally reported strain effect is generated by compressing or expanding the nanostructure to make the atomic arrangement of the surface layer.[15,19–21] The strain effect at the atomistic scale can lead to the change in lattice parameter, and alter the intrinsic interatomic distances and modify the energy levels of the bonding electrons. To date, different strategies have been explored to generate the surface strain in catalytic materials through application of an external force, physically bending, or stretching the supporting substrate and thermomechanically deforming a shape-memory alloy substrate.[22–25] However, the surface strain only tends to compress to a larger extent on nanocrystals with a smaller size (<5 nm) due to the high surface area to volume ratio and highly curved surfaces, allowing the stress to be distributed over a large fraction of the constituent atoms. By controlling the size of the nanomaterial to tune the surface strain with compromising other structural properties is not very useful in electrocatalysis. Therefore, a new strategy toward the development of controllable approaches to introduce and modulate strain to a desired level on the surface of electrocatalysts is highly desirable. Furthermore, correlating induced strain with catalytic performance is of fundamental importance, and such a mechanistic study of the strain–performance relationship requires the capability of inducing surface strain on catalysts as precisely as possible, however, achieving the precise strain on nanocatalysts has never been demonstrated.

Herein, we report a conceptually new strategy to generate the precise and tunable tensile strain through introducing 2D 2H-MoS_2 with precisely controllable layers onto cubic Co_9S_8 nanocrystals. The lattice strains are induced by the epitaxial growth of lattice-mismatched structure when the MoS_2 layer is coherently grown on a compressible Co_9S_8 core. The atomic-scale shell number engineering in outer MoS_2 from 1L to 5L leads to the gradual changes in tensile lattice strain from 3.5% to 0% for MoS_2, significantly regulating the adsorption properties of rate-limiting intermediates, and eventually determining the catalytic properties. The Co_9S_8/1L MoS_2 with 3.5% tensile strain exhibits superior HER activity with an overpotential of 95 mV at current density of 10 mA cm^{-2} and a Tafel slope of 71 mV $decade^{-1}$, originating from the complex interplay of strain effects through the S atom bonding interaction. Theoretical calculations and experimental results demonstrate that the heteroepitaxial lattice-strain can be used to tune the charge transfer and energy barriers of hydrogen atom absorption (ΔE_H) and energy barrier for the transition state 2H* (ΔE_{2H*}). The optimized bandgap (closer to the Fermi level) with tensile strain of 3.5% and enhanced charge density at Co—S—Mo interface with the covalent bonding character and electron redistribution yield the ΔE_H of −1.03 eV and ΔE_{2H*} of 0.29 eV (MoS_2, ΔE_H = −0.86 eV and ΔE_{2H*} = 0.49 V), which are the key in boosting HER activity by stabilizing the HER intermediate, seizing H ions and releasing H_2 gas. Our work establishes a new relationship between the tensile lattice strain and HER performance, offering great convenience in correlating the structural properties and surface reactivity of strained core/shell electrocatalytic nanomaterials.

The Co_9S_8/MoS_2 core/shell nanocrystals supported on carbon nanofibers (Co_9S_8/MoS_2-CNFs) were in situ synthesized via S vapor-assisted methods without adding any capping and reducing agents. The Co_9S_8/MoS_2 with different MoS_2 layer numbers were defined as Co_9S_8/nL MoS_2 (n = 1–5). The synthetic process and structure evolutions of Co_9S_8/nL MoS_2 were shown in **Scheme 1** (details in Figure S1 in the Supporting Information). Figure S2 in the Supporting Information shows field-emission scanning electron microscopy (FESEM) and transmission electron microscopy (TEM) images of Co_9S_8/1L MoS_2 core/shell nanocrystals. They employ the octahedral shape with an average diameter of ≈35 nm. The individual MoS_2 exhibits 2D nanoplate morphology, and the Co_9S_8 displays octahedral structure (Figures S3 and S4, Supporting Information). FESEM and high-resolution TEM (HRTEM) images of Co_9S_8/1L MoS_2 core/shell nanocrystals (**Figure 1**a,b)

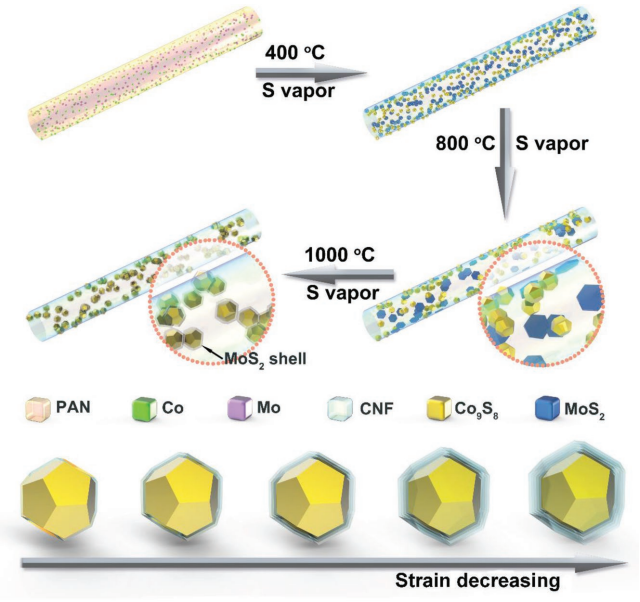

Scheme 1. Synthetic process for Co_9S_8/MoS_2 core/shell nanocrystals with precisely controlled shell numbers supported on CNFs.

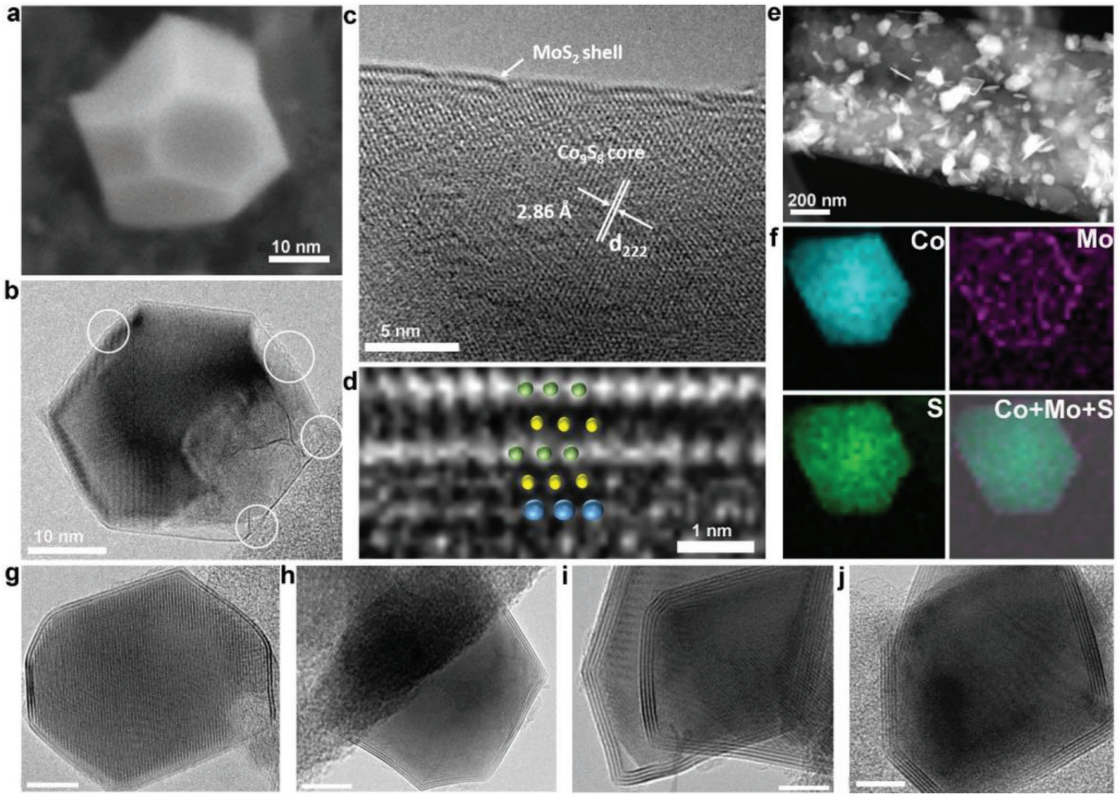

Figure 1. High magnification a) SEM and b) TEM images of single Co_9S_8/1L MoS_2 nanocrystal. c) HRTEM image of one side edge of the Co_9S_8/1L MoS_2 and d) Co—S—Mo nanointerface. e) HAADF-STEM and f) STEM-EDX mapping images of Co_9S_8/1L MoS_2 supported on CNFs. HRTEM images of Co_9S_8/nL MoS_2 nanocrystals with different MoS_2 shell numbers: g) 2L, h) 3L, i) 4L, and j) 5L. Scale bars 5 nm.

shows that the Co_9S_8 core is confined into monolayer MoS_2. The edge of Co_9S_8/1L MoS_2 exhibits only one layer, and the Co_9S_8 core exhibits well-defined lattice fringe with space of 2.86 Å, being consistent with the (222) planes of the cubic Co_9S_8 phase (Figure 1c). HRTEM image (Figure 1d) clearly shows the formation of Co—S—Mo atomic interface (The chemical model of Co_9S_8/1L MoS_2 shows that the S atoms bridge Co and Mo atoms to form nanointerfaces, Figure S5, Supporting Information). The high-angle annular dark-field scanning transmission electron microscopy (HAADF-STEM, Figure 1e,f) and corresponding elemental mapping images indicate that the Co element is uniformly distributed in the inner particle, and completely surrounded by the Mo element. The overlap element mappings provide direct evidence for the formation of a core/shell structure in the nanocrystals, in which a MoS_2 shell surrounds a Co_9S_8 core.

This strategy can be employed to design a series of Co_9S_8/MoS_2 core/shell nanocrystals with precisely controlled layer numbers. Figure 1g–j shows that the shell layer number of Co_9S_8/MoS_2 core/shell structure can be easily tuned from 2L to 5L by adjusting the MoS_2 content (mass ratio from 5% to 30%). HRTEM image of Co_9S_8/3L MoS_2 (Figure S6, Supporting Information) displays the visible lattice fringe with a space of 6.5 Å, corresponding to the (002) plane of the 2H-MoS_2. The density functional theory (DFT) calculations were used to investigate the lattice strains induced by atomic scale engineering in core/shell structures. We used the Co_9S_8/nL MoS_2 (n = 1–3) as the calculated sample. The chemical structure models of Co_9S_8, MoS_2, Co_9S_8/nL MoS_2 (n = 1–3) (Figures S7 and S8, Supporting Information) indicate that all the interfaces between MoS_2 and Co_9S_8 are bonded by S atoms in MoS_2 layer. Figure S9 in the Supporting Information illustrates the bond angles of Co—S and Mo—S for Co_9S_8, MoS_2, and Co_9S_8/nL MoS_2 (n = 1–3), respectively. It is indicated that the increased MoS_2 layers lead to the continuously adjustment of the bond angles of Co—S and Mo—S, further resulting in the enlarged Mo—S bond lengths from 2.412 Å in monolayer MoS_2 to 2.454–2.507 Å in core/shell structure (calculated by DFT, Figure S9, Supporting Information). The lattices ($a \times b$) of MoS_2 and Co_9S_8 are optimized to be 6.36 × 11.01 Å and 6.93 × 11.99 Å, respectively. The strain (τ) for Co_9S_8/nL MoS_2 is defined as

$$\tau = \frac{a_{Co_9S_8/MoS_2} - a_{MoS_2}}{a_{MoS_2}} \quad (1)$$

The Co_9S_8/nL MoS_2 is built as 2 × 2 orthorhombic MoS_2 supercells by attaching the MoS_2 slab onto the (111) planes of Co_9S_8. As illustrated in Figure S10 in the Supporting Information, the lattice strain changes from 3.5% to 1.3% by controlling the number of MoS_2 layers from 1L to 3L. The lattice parameters and strains of Co_9S_8/nL MoS_2 (n = 1–3) were shown in Table S1 in the Supporting Information. The atomic scale engineering in MoS_2 shell varied from 1L to 3L makes the lattice parameters of MoS_2 shifted to smaller values (3.5% to 1.3%).

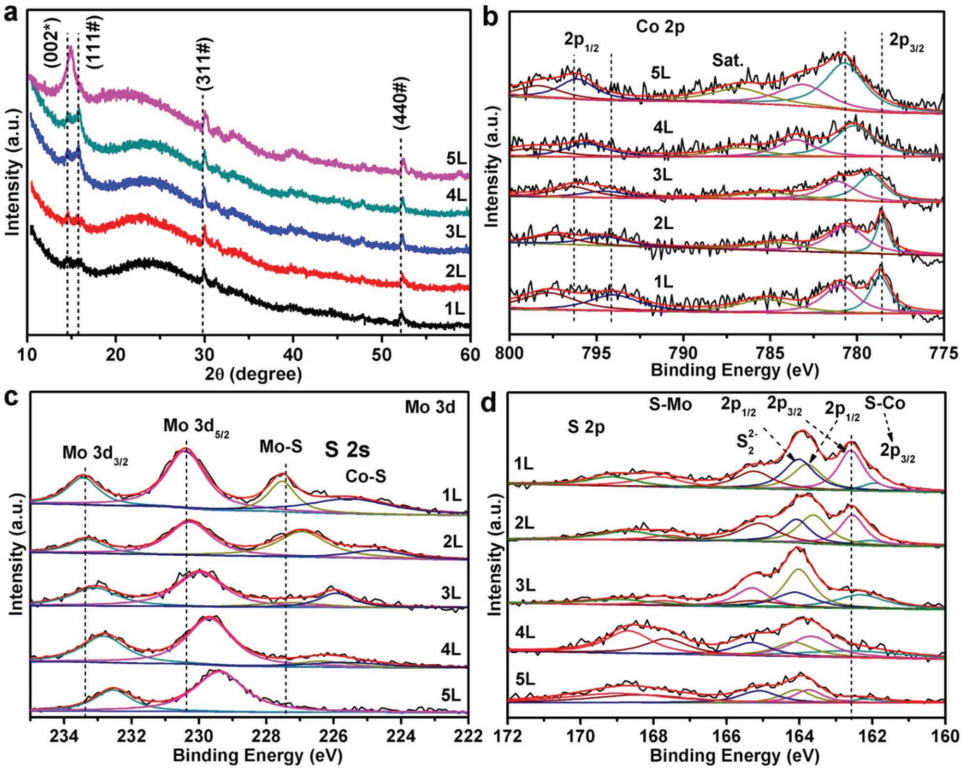

Figure 2. a) XRD patterns of the Co_9S_8/nL (n = 1–5) MoS_2 with designed MoS_2 shell. b) Co 2p, (c) Mo 3d, and (d) S 2s XPS spectra of the Co_9S_8/nL MoS_2 (n = 1–5) supported on CNFs.

Figure S11 in the Supporting Information shows the X-ray diffraction patterns of MoS_2, Co_9S_8, and Co_9S_8/1L MoS_2. Two series of Bragg reflections, emerged in Co_9S_8/1L MoS_2, correspond to the 2H MoS_2 (marked with *, JCPDS 37–1492) and fcc Co_9S_8 phases (marked with #, JCPDS No. 86–2273), respectively.[26,27] The characteristic peaks for Co_9S_8/1L MoS_2 core/shell structures exhibit significant shifts compared with those of individual Co_9S_8 and MoS_2. **Figure 2**a shows the X-ray diffraction (XRD) patterns of Co_9S_8/nL MoS_2 with tunable MoS_2 layers (n = 1–5). The diffraction peaks of Co_9S_8 in Co_9S_8/n MoS_2 core/shell nanocrystals shift to higher degree, suggesting the MoS_2 shell would compress the crystal lattice of Co_9S_8, leading to the decrease of the crystal lattice constant. In this regard, the lattice strain for both MoS_2 and Co_9S_8 in core/shell structure can be tuned through the atomic scale structure engineering. The diffraction peaks change for Co_9S_8, MoS_2, and Co_9S_8/nL MoS_2 (n = 1–5) are summarized in Table S2 in the Supporting Information.

X-ray photoelectron spectroscopy (XPS) was used to investigate the charge transfer at the Co—S—Mo atomic interface aroused by two dissimilar surfaces of Co_9S_8 and MoS_2. Figure 2b shows the Co 2p XPS spectra of Co_9S_8/nL MoS_2 with tunable MoS_2 shells (n = 1–5). All of them exhibit two spin–orbit doublets and shake-up satellites (marked as "Sat."). The first doublet of Co_9S_8/1L MoS_2 emerges at 778.5 and 794.0 eV while the second doublet is located at 781.1 and 797.8 eV, corresponding to the spin–orbit splitting value of Co $2p_{1/2}$ and Co $2p_{3/2}$ for Co^{3+} and Co^{2+}, respectively.[28–30] The Mo 3d XPS spectrum of Co_9S_8/1L MoS_2 (Figure 2c) displays two predominant peaks located at 230.4 and 233.4 eV, corresponding to the Mo $3d_{5/2}$ and Mo $3d_{3/2}$ of Mo (VI).[31–33] The S 2s exhibits two chemical states located at 227.5 and 225.3 eV, ascribed to the chemical bonds of Co—S and Mo—S. Importantly, the binding energies (BEs) for Co peaks shift to a higher energy along with the Mo peaks shifting to a lower energy, which is induced by the MoS_2 shell growth. The significant BE shifts in XPS spectra of Co, Mo, and S suggest the strong charge transfer from the Co atom to Mo atom through the Co—S—Mo atomic interface, leading to the increased electron density. Multilayered MoS_2 shells in core/shell structure would obstruct the charge transfer from the Co atom to Mo atom (Figures S12 and S13, Supporting Information). As illustrated in Figure 2d, the S 2p spectrum of the Co_9S_8/1L MoS_2 displays two doublets for S $2p_{3/2}$ and S $2p_{1/2}$ located at 161.9, 163.8, and 162.6, 164.1 eV, respectively, ascribed to the typical coordination of sulfur ions with Co and Mo metal ions. The emerged peak at 165.3 eV suggests the existence of bridging disulfides S_2^{2-} and/or apical S^{2-} ligands.[39–42] The high BEs at 167.8 and 169.1 eV can be assigned to C—S—C and S (VI) species in sulfate groups (SO_3^{2-}), respectively.

To obtain a deeper insight into the atom-level engineering in the core/shell structures, a series of control experiments were conducted. We focused on the growth process controlled by temperatures from 600 to 1000 °C. **Figure 3**a shows that only a small monolayer MoS_2 was heteroepitaxially bonded onto the surface of Co_9S_8 cores at 600 °C. By further increasing the temperature to 800 and 1000 °C, the surfaces of Co_9S_8 cores were continuously bonded by monolayer MoS_2 to form a completely shell (Figure 3b,c), indicating the thermodynamics-driven

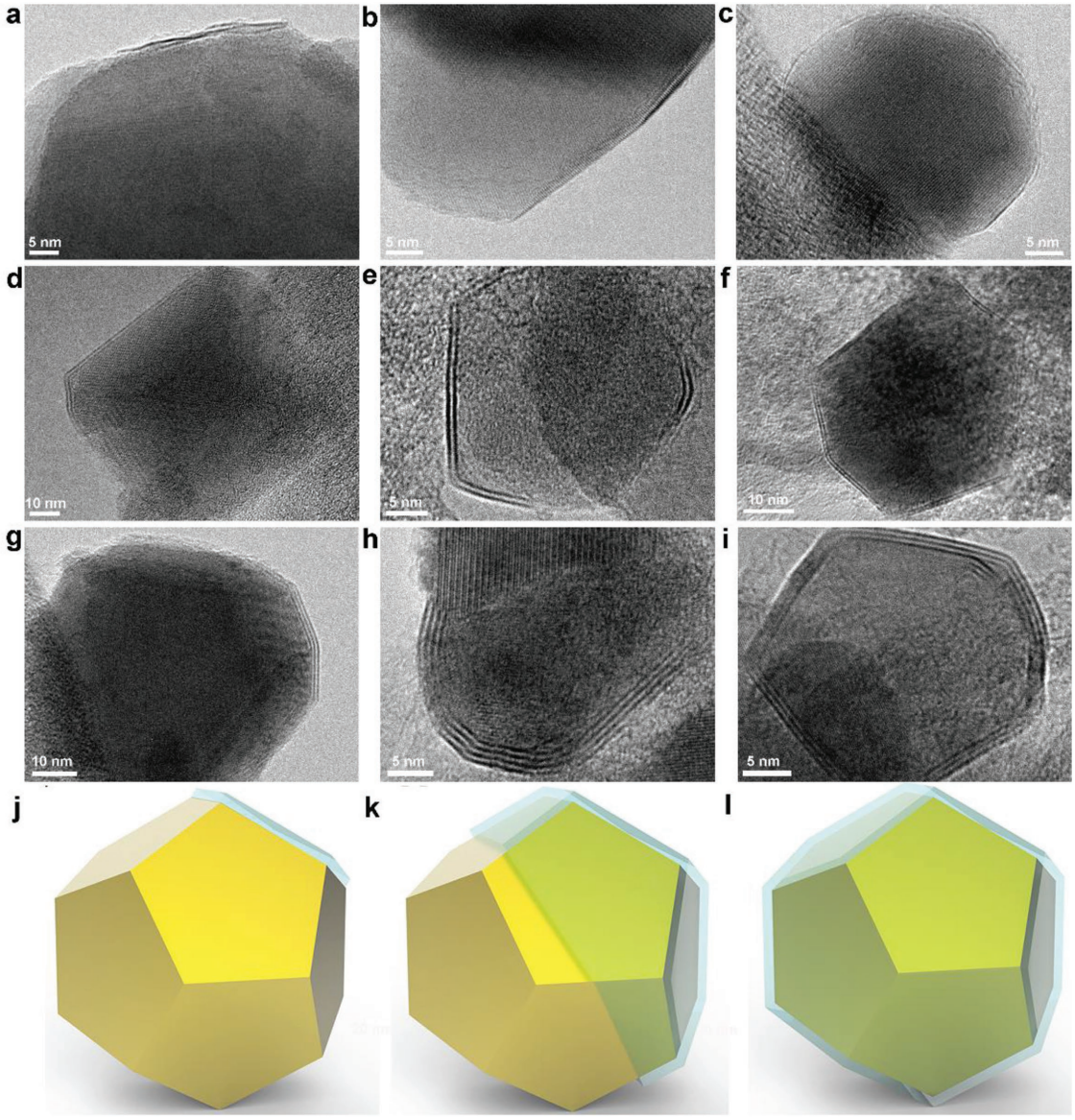

Figure 3. TEM images of Co_9S_8/1L MoS_2, Co_9S_8/2L MoS_2, and Co_9S_8/3L MoS_2 prepared at different graphitization temperatures of (a,d,e) 600 °C, (b,e,h) 800 °C, and (c,f,i) 1000 °C. j–l) Schematic illustration of the structure evolutions of Co_9S_8/1L MoS_2 under different temperatures.

growth process. Similarly, for Co_9S_8/2L MoS_2 (Figure 3d–f) and Co_9S_8/3L MoS_2 (Figure 3g–i), the MoS_2 shells with corresponding layer numbers were also driven onto Co_9S_8 surface, and then gradually grown to a completely core/shell structures. The proposed growth mechanism was illustrated in Figure 3g–l. The Co and Mo precursors were first decomposed onto individual MoS_2 nanoplate and Co_9S_8 nanoparticles at low temperature (400 °C). Through the thermodynamics driven, the MoS_2 nanoplates were gradually heteroepitaxial bonded onto the Co_9S_8 surfaces by the S atom bridge. The heteroepitaxial coverage extent of MoS_2 shell on Co_9S_8 surfaces can be tuned by changing the graphitization temperatures (600–1000 °C).

The electrochemical performance of the Co_9S_8/nL MoS_2 (n = 1–5) core/shell nanocrystals with controlled MoS_2 shell number were investigated via a three-electrode setup in 0.5 M H_2SO_4 solution. **Figure 4**a,b demonstrates the polarization curves of Co_9S_8/nL MoS_2 (n = 1–5) core/shell nanocrystals supported on CNFs and commercial Pt/C at the scan rate of 2 mV^{-1}. The overpotential (η) at 10 mA cm^{-2} is frequently used as an important metric to evaluate the electrochemical performance (Figure 4b). The Co_9S_8/1L MoS_2-CNFs show an overpotential (η) of 95 mV versus reversible hydrogen electrode (RHE) at current density of 10 mA cm^{-2}, much lower than those of Co_9S_8/MoS_2 with layer number from 2 to 5 (124, 175, 181, and 208 mV, respectively), indicating that multilayered MoS_2 shells would result in the low HER activity. The η value of Co_9S_8/1L MoS_2 is close to that of commercial Pt/C catalyst (55 mV), and comparable or even superior to those of reported non-noble metal catalysts (Table S3, Supporting Information). Tafel plots (Figure 4c,d) further show the superiority of Co_9S_8/1L MoS_2 (71 mV dec^{-1}) over the other Co_9S_8/nL MoS_2 core/shell with n from 2 to 5 (92, 101, 108, 145 mV dec^{-1}, respectively) with

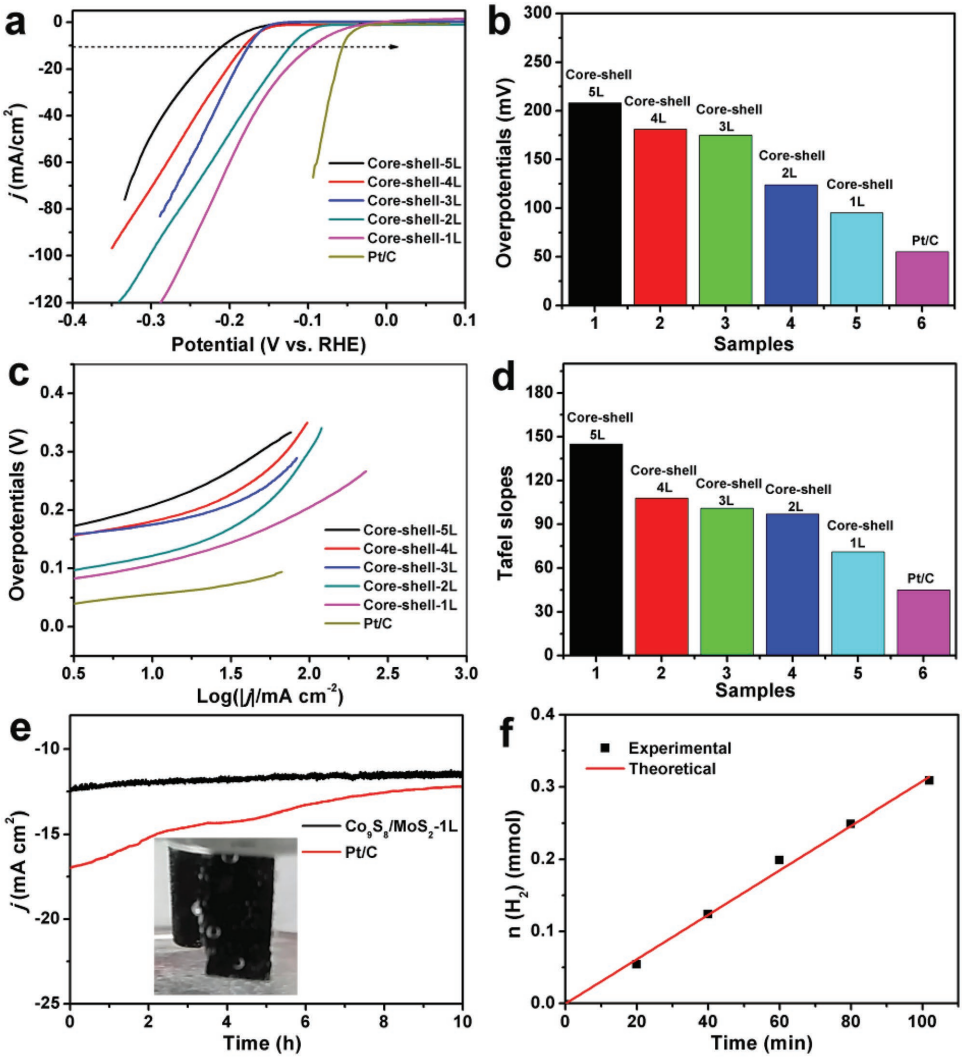

Figure 4. a) Polarization curves of Co_9S_8/nL MoS_2 (n = 1–5) core/shell nanocrystals supported on CNFs and commercial Pt/C catalyst in 0.5 M H_2SO_4. Scan rate: 2 mV s^{-1}. b) Overpotentials of various Co_9S_8/nL MoS_2-CNFs (n = 1–5) catalysts and commercial Pt/C for HER at the current density of 10 mA cm^{-2}. c,d) Tafel plots of the Co_9S_8/nL MoS_2 (n = 1–5)-CNFs and Pt/C catalysts. e) Long-term durability test of core/shell Co_9S_8/1L MoS_2-CNFs and Pt/C catalysts for HER at –0.31 V versus the reversible hydrogen electrode (RHE) in 0.5 M H_2SO_4. Inset is the photograph of the electrode. f) The theoretically calculated (red line) and experimental (black cubes) amount of hydrogen produced by the Co_9S_8/1L MoS_2 as a function of time.

regard to HER kinetics (Table S4, Supporting Information). The Tafel plot value of Co_9S_8/1L MoS_2 is 71 mV dec^{-1}, suggesting a Volmer–Heyrovsky reaction path, which means that the electrochemical hydrogen desorption is the rate-limiting step. The electrolysis experiment was further measured quantitatively by gas chromatography, and there are negligible difference between the amount of experimentally quantified H_2 (black cubes) and the theoretically calculated one (red line), indicating extremely low loss in Faradaic efficiency, which is close to 100% for the Co_9S_8/1L MoS_2-CNFs (Figure 4f). In addition, the η values of pure Co_9S_8/CNFs (Figure S14, Supporting Information) and 1L MoS_2-CNFs (Figure S14, Supporting Information) are 304 and 221 mV, respectively and the corresponding Tafel slopes are 140 and 110 mV dec^{-1}, suggesting their poor intrinsic HER activity. Furthermore, the double-layer capacitance (C_{dl}) values of Co_9S_8/1L MoS_2-CNFs were calculated to be 23.4 mF cm^{-2} (Figure S15, Supporting Information), superior to those of other Co_9S_8/nL MoS_2 core/shell with n from 2 to 5 (12.4, 9.8, 6.7, and 1.4 mF cm^{-2}, respectively). This result demonstrates the Co_9S_8/1L MoS_2 has much more exposed catalytic sites.

Figure 4e shows the chronoamperometry (i–t) curve of Pt/C and Co_9S_8/1L MoS_2-CNFs electrode performed at –0.31 V versus RHE in 0.5 M H_2SO_4 over 10 h. The Co_9S_8/1L MoS_2-CNFs electrode delivers a stabilized HER current density of ≈10 mA cm^{-2}. The current density of the Co_9S_8/1L MoS_2-CNFs electrode retains 90% while only 75% of the current density of Pt/C remains under the same condition, suggesting the better stability of Co_9S_8/1L MoS_2-CNFs against HER. In the durability cycle test, the linear sweep voltammetry (LSV) curves of Co_9S_8/1L MoS_2 show no significant decay after 1000 cycles, suggesting its robust catalytic activity (Figure S16, Supporting Information). This conclusion was further proved by the fact that there are almost no morphology and structure changes for the Co_9S_8/1L MoS_2-CNFs after stability tests (Figures S17–19, Supporting Information).

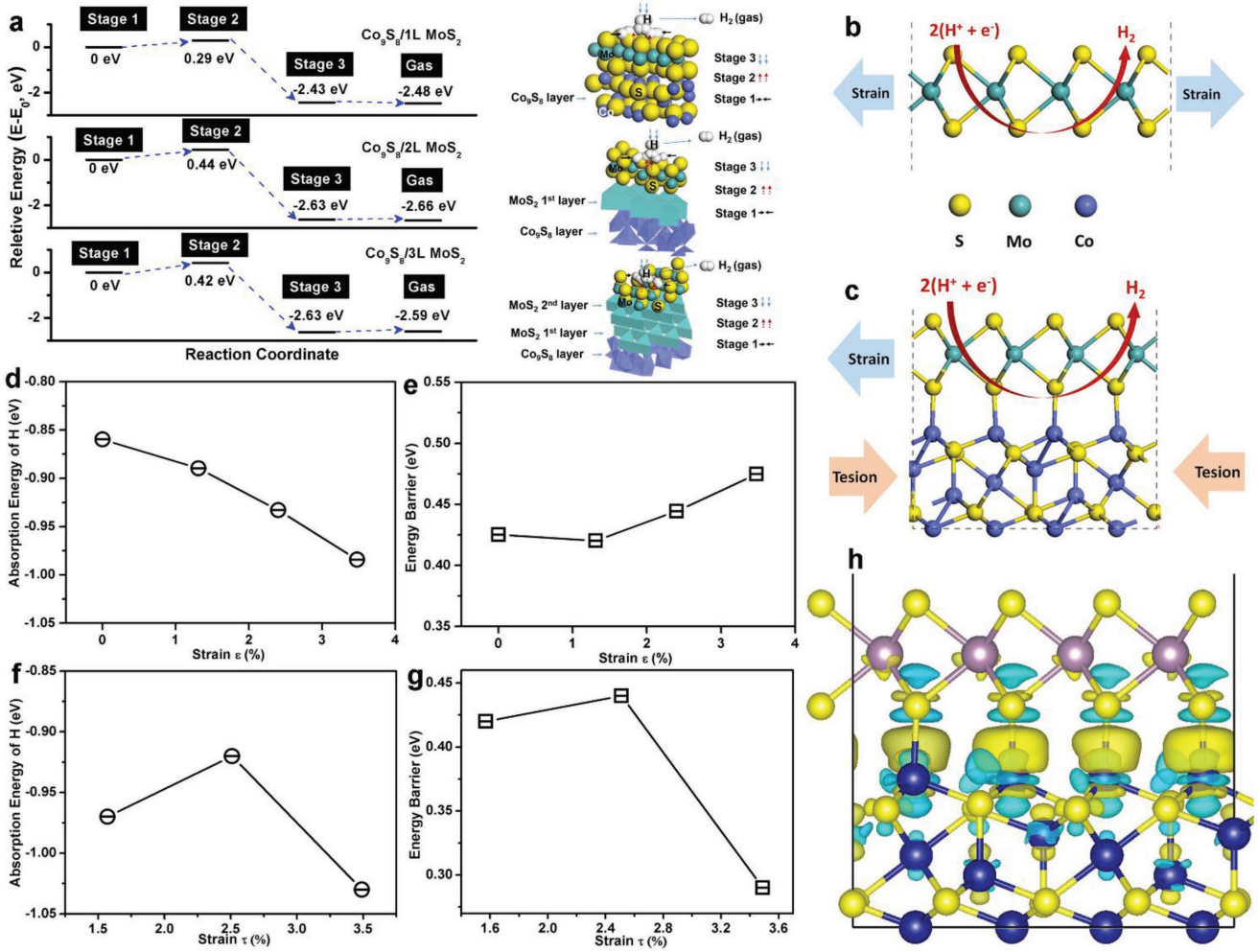

Figure 5. a) Reaction pathways of hydrogen atom adsorption and hydrogen molecule desorption on Co_9S_8/1L MoS_2, Co_9S_8/2L MoS_2, and Co_9S_8/3L MoS_2 for HER. Chemical models of the strained (b) MoS_2 and (c) Co_9S_8/1L MoS_2 core/shell nanostructure. The calculated (d) ΔE_H and (e) ΔE_{2H^*} for the strained MoS_2 versus the %ε strain. The calculated (f) ΔE_H and (g) ΔE_{2H^*} for strained Co_9S_8/1L MoS_2 core/shell versus the % τ strain. h) Electron density differences at Co—S—Mo nanointerface in Co_9S_8/1L MoS_2. Yellow density means positively charged and blue density means negatively charged.

In order to investigate the relationship between the lattice strain and the HER activity, we investigated the kinetic energy barrier profiles of HER on the MoS_2 and Co_9S_8/nL MoS_2 (n = 1–3) surfaces using the climbing-image nudged elastic band[34] method implemented in vienna ab initio simulation package[35,36] (**Figure 5**a). In this work, the Tafel value of Co_9S_8/1L MoS_2 is 71 mV dec^{-1}, indicating a Volmer–Heyrovsky reaction path, and the electrochemical hydrogen desorption is the rate-limiting step.[37–39] According to the transition state theory, we can divide the HER process as follows: the adsorption of hydrogen atoms (Stage 1), the transition state of 2H* into H_2 (Stage 2), the formation of H_2 on catalyst surfaces (Stage 3), and the desorption of H_2 from the catalyst surfaces. The hydrogen adsorption energy (ΔE_H) determines the capability of catalyst to bond the hydrogen atoms. The conversion from H to H_2 through the transition state 2H* on catalyst surfaces should overcome the energy barrier of transition state 2H* (ΔE_{2H^*}) between Stage 1 and Stage 2. In the Eyring equation,[40,41] the chemical kinetics relies on the reaction rate (K), while the reaction speed is mainly determined by the energy barrier of transition state with constant reaction temperature, according to Equation (2)

$$K = \frac{-\mathrm{d}[\mathrm{H}]}{\mathrm{d}t} = \frac{k_b T}{h} \exp\left\{\frac{-\Delta E_{2H^*}}{RT}\right\} \quad (2)$$

"T" equals the temperature, "k_b" equals the Boltzmann constant, "h" equals Planck's constant, "ΔE_{2H^*}" is the energy barrier of transition state and "R" is the gas constant.

The energy barrier of transition state (ΔE_{2H^*}) determines the formation and desorption of hydrogen molecule. Therefore, the overall HER activity largely depends on the hydrogen adsorption energy (ΔE_H) and especially the energy barrier of transition state 2H* (ΔE_{2H^*}). This work proposes a new strategy to both optimize the ΔE_H and ΔE_{2H^*} through precisely tuning tensile lattice strain induced by atomic scale engineering in core/shell structure. Herein, a theoretical study was systematically applied to identify the biaxial strain effect on the adsorption,

diffusion, and molecular dissociation of hydrogen on the MoS_2 and Co_9S_8/nL MoS_2 (n = 1–3) core/shell nanocrystals with controlled tensile lattice strains.

The adsorption energies of H and H_2 on the surface of MoS_2 and Co_9S_8/nL MoS_2 (n = 1–3) surfaces were derived as

$$\Delta E_{\mathrm{H}} = \frac{1}{n}\left(E(\mathrm{surf}+n\mathrm{H}) - E(\mathrm{surf}) - nE(\mathrm{H})\right) \quad (3)$$

$$\Delta E_{H_2} = \frac{1}{n}\left(E(surf+nH_2) - E(surf) - nE(H_2)\right) \quad (4)$$

where n is the number of adsorbed hydrogen atoms, E(surf) is the total energy of the surface without H adsorption, and E (surf + n H) is the total energy of the surface with n adsorbed atoms or molecules.

We used the DFT calculations to show the effects of lattice strains in the ΔE_{H} and $\Delta E_{2\mathrm{H}^*}$ of pure 2H MoS_2 and Co_9S_8/nL (n = 1–3) MoS_2 core/shell nanocrystals. The process for activating the basal plane of pure MoS_2 through the strain (defined as strained MoS_2) is illustrated in Figure 5b,c. The ΔE_{H} largely depends on the bandgap and the number of gap states around Fermi level.[13] The electronic structure can be manipulated by straining the MoS_2 surface, as illustrated in Figure S20 in the Supporting Information. The strains (ε) on MoS_2 are divided four equal proportions, where strain (ε) is defined as

$$\varepsilon = \frac{a_{\text{strained } MoS_2} - a_{MoS_2}}{a_{MoS_2}} \quad (5)$$

The geography of the four configurations of strained MoS_2 was optimized, as shown in Table S5 in the Supporting Information. For MoS_2 without strain, all the angles are same with a standard deviation value (V_{StdDev}) of zero. Higher strains lead to larger Mo—S—Mo angles and V_{StdDev}, indicating the structure distortion. For the H atom adsorption positions on strained MoS_2 with range of 0–3.5%, there are one H atom perpendicular to the plane, and the other one parallel to the plane. The optimized structures of the MoS_2 and H-MoS_2 and H_2-MoS_2 are shown in Figure S21 in the Supporting Information. The larger strains in MoS_2 make the hydrogen binding energy more negative ΔE_{H} (from –0.85 to –0.98 eV), indicating the enhanced capability for adsorbing hydrogen atoms on the strained MoS_2 surfaces (Figure 5d; Table S6, Supporting Information). The band structure calculations for the strained MoS_2 are shown in Figure S14 in the Supporting Information, using pure MoS_2 as standard semiconductors with indirect bandgap of 1.94 eV. The larger strains lead to the shifts of band to Fermi level gradually (Figure S22, Supporting Information) without new band appearance, which strengthen the hydrogen binding, being in accordance with the ΔE_{H} results (Figure 5d). As illustrated in Figure 5e, the $\Delta E_{2\mathrm{H}^*}$ exhibits the opposite trend (0.42 to 0.47 eV) with increased MoS_2 strains, indicating that directly strengthening the lattice strain in pure 2H MoS_2 does not obtain the optimal ΔE_{H} and $\Delta E_{2\mathrm{H}^*}$.

We have calculated the ΔE_{H} and $\Delta E_{2\mathrm{H}^*}$ for Co_9S_8/nL MoS_2 (n = 1–3) core/shell nanocrystals with controlled strain from 1.3% to 3.5% (Figure 5f,g). The optimized structures of the H(2)–Co_9S_8/n MoS_2 (n = 1, 2, 3) are shown in Figures S23 and S24 in the Supporting Information. For the adsorption of one H atom, there is only one perpendicular H—S bond for all Co_9S_8/nL MoS_2 (n = 1–3). The Co_9S_8/2L MoS_2 and Co_9S_8/3L MoS_2 exhibit similar $\Delta E_{2\mathrm{H}^*}$ of 0.44 and 0.42 eV during Stage 2. Compared with the strained MoS_2, the Co_9S_8/1L MoS_2 exhibits the lowest ΔEH of –1.03 eV and $\Delta E_{2\mathrm{H}^*}$ of 0.29 eV with a strain of 3.5%, indicating that the designed core/shell structures have strong positive effects on ΔE_{H} and $\Delta E_{2\mathrm{H}^*}$. In addition, the ΔEH for the strained MoS_2 and Co_9S_8/nL MoS_2 (n = 1–3) decreases with the increasing strain from 1.3% to 3.5%, indicating that the hydrogen adsorption energy can be tuned by the lattice strains (Table S7, Supporting Information).

To further study the exceptional changes of energy barrier for all strains, we have investigated the charge transfer between H and MoS_2 surface at Stage 2 through the charge density difference ($\Delta\rho(r)$) method, where yellow density means positively charged and blue density means negatively charged. As shown in Figure S25 in the Supporting Information, for pure MoS_2, one of the H atoms loses extra electrons to form negative charge center, and the S atom adjacent to H atom absorbs electrons to form positive center. But the other H atom absorbs extra electrons, which decreases the interaction with the neighbor S atom, leading to a higher ΔE_{H} in the transition state (Stage 2). As shown in Figure 5h, for the Co_9S_8/1L MoS_2 with the strain of 3.5%, blue charge density on the S and Co atoms at the Co—S—Mo interface means a negative charging, and yellow one on Mo atoms means positive charging, being in good agreement with XPS results. Both two H atoms transfer electrons to the S atoms nearby, which can decrease the $\Delta E_{2\mathrm{H}^*}$ and form lower energy barrier. The charge density at Co—S—Mo interface indicates the covalent bonding character and electron redistribution on the surface as a consequence. The Co_9S_8/1L MoS_2 surfaces exhibit the lowest ΔE_{H} of –1.03 eV and $\Delta E_{2\mathrm{H}^*}$ of 0.29 eV among the strained MoS_2 and Co_9S_8/nL MoS_2 (n = 2, 3), indicating the highest active nature of monolayer MoS_2 on Co_9S_8 in stabilizing the HER intermediate, seizing H ions and releasing H_2 gas. In the core/shell structure, the induced lattice strain together with the enhanced charger density at Co—S—Mo nanointerfaces not only facilitates the initial hydrogen adsorption but also expedites the subsequent water dissociation, cooperatively resulting in the significant promotion of HER activity. The results establish a new strain–reactivity relationship, offering great convenience in correlating the structural properties and surface reactivity of new strain-controlled electrocatalytic nanomaterials.

In conclusion, we demonstrate a concept of manipulating the hydrogen adsorption energy and kinetic energy barrier for transition state 2H* to boost HER activity by creating precise tensile surface strain in Co_9S_8/MoS_2 core/shell nanocrystals. The lattice strains were induced by the heteroepitaxial growth of lattice-mismatched structures when the MoS_2 layer is coherently grown on a compressible Co_9S_8 core. The lattice strain can be tuned from 0% to 3.5% for MoS_2 by the atomic-scale structure engineering in outer MoS_2 shell numbers from 5L to 1L. DFT results indicate that the large tensile surface strain of 3.5% from Co_9S_8/1L MoS_2 core/shell nanocrystals can produce the optimized bandgap (closer to the Fermi level), and allow favorable hydrogen adsorption and fast diffusion process, yielding the optimal ΔE_{H} of –1.03 eV and $\Delta E_{2\mathrm{H}^*}$ of 0.29 eV,

which are the key in enhancing HER catalysis herein. Our work demonstrates the first example in establishing a new strain–reactivity relationship in tensile strain-controlled electrocatalytic nanomaterials.

Supporting Information

Supporting Information is available from the Wiley Online Library or from the author.

Acknowledgements

H.Z. and G.G. contributed equally to this work. This study was supported by the National Natural Science Foundation of China (NSFC) (Grant nos. 51373154, 51573166, 51472182, U1503292, 71371143, 51671003), the MOE & SAFEA, 111 Project (B13025), the National Basic Research Program of China (No. 2017YFA0206701), Open Project Foundation of State Key Laboratory of Chemical Resource Engineering, the start-up supports from Peking University and Young Thousand Talented Program, the national first-class discipline program of Light Industry Technology and Engineering (LITE2018-19), and the Fundamental Research Funds for the Central Universities.

Conflict of Interest

The authors declare no conflict of interest.

Keywords

electrocatalysis, hydrogen evolution, materials chemistry, structure engineering, tensile strain

Received: December 14, 2017
Revised: February 25, 2018
Published online:

[1] S. Chu, A. Majumdar, *Nature* **2012**, *488*, 294.
[2] Z. Cao, Q. Chen, J. Zhang, H. Li, Y. Jiang, S. Shen, G. Fu, B. Lu, Z. Xie, L. Zheng, *Nat. Commun.* **2017**, *8*, 15131.
[3] C. Bae, T. A. Ho, H. Kim, S. Lee, S. Lim, M. Kim, H. Yoo, J. M. Montero-Moreno, J. H. Park, H. Shin, *Sci. Adv.* **2017**, *3*, e1602215.
[4] A. Z. Haddad, B. D. Garabato, P. M. Kozlowski, R. M. Buchanan, C. A. Grapperhaus, *J. Am. Chem. Soc.* **2016**, *138*, 7844.
[5] O. Khaselev, J. A. Turner, *Science* **1998**, *280*, 425.
[6] G. Li, D. Zhang, Q. Qiao, Y. Yu, D. Peterson, A. Zafar, R. Kumar, S. Curtarolo, F. Hunte, S. Shannon, Y. Zhu, W. Yang, L. Cao, *J. Am. Chem. Soc.* **2016**, *138*, 16632.
[7] M. S. Faber, S. Jin, *Energy Environ. Sci.* **2014**, *7*, 3519.
[8] J. D. Benck, T. R. Hellstern, J. Kibsgaard, P. Chakthranont, T. F. Jaramillo, *ACS Catal.* **2014**, *4*, 3957.
[9] H. Wang, S. Min, Q. Wang, D. Li, G. Casillas, C. Ma, Y. Li, Z. Liu, L. J. Li, J. Yuan, M. Antonietti, T. Wu, *ACS Nano* **2017**, *11*, 4358.
[10] Y. Yin, J. Han, Y. Zhang, X. Zhang, P. Xu, Q. Yuan, L. Samad, X. Wang, Y. Wang, Z. Zhang, P. Zhang, X. Cao, B. Song, S. Jin, *J. Am. Chem. Soc.* **2016**, *138*, 7965.
[11] A. M. Smith, A. M. Mohs, S. Nie, *Nat. Nanotechnol.* **2009**, *4*, 56.
[12] E. M. Gallego, M. T. Portilla, C. Paris, A. León-Escamilla, M. Boronat, M. Moliner, A. Corma, *Science* **2017**, *355*, 1051.
[13] H. Li, C. Tsai, A. L. Koh, L. Cai, A. W. Contryman, A. H. Fragapane, J. Zhao, H. S. Han, H. C. Manoharan, F. Abild-Pedersen, J. K. Nørskov, X. Zheng, *Nat. Mater.* **2016**, *15*, 48.
[14] M. Cabán-Acevedo, M. L. Stone, J. R. Schmidt, J. G. Thomas, Q. Ding, H. C. Chang, M. L. Tsai, J. He, S. Jin, *Nat. Mater.* **2015**, *14*, 1245.
[15] P. Strasser, S. Koh, T. Anniyev, J. Greeley, K. More, C. Yu, Z. Liu, S. Kaya, D. Nordlund, H. Ogasawara, M. F. Toney, A. Nilsson. *Nat. Chem.* **2010**, *2*, 454.
[16] D. Voiry, H. Yamaguchi, J. Li, R. Silva, D. C. B. Alves, T. Fujita, M. Chen, T. Asefa, V. B. Shenoy, G. Eda, M. Chhowalla, *Nat. Mater.* **2013**, *12*, 850.
[17] M. Luo, S. Guo, *Nat. Rev. Mater.* **2017**, *2*, 17059.
[18] M. Gsell, P. Jakob, D. Menzel, *Science* **1998**, *280*, 717.
[19] M. R. Nellist, F. A. Laskowski, F. Lin, T. J. Mills, S. W. Boettcher, *Acc. Chem. Res.* **2016**, *49*, 733.
[20] S. Ismail-Beigi, F. J. Walker, A. S. Disa, K. M. Rabe, C. H. Ahn, *Nat. Rev. Mater.* **2017**, *2*, 17060.
[21] W. J. Huang, R. Sun, J. Tao, L. D. Menard, R. G. Nuzzo, J. M. Zuo, *Nat. Mater.* **2008**, *7*, 308.
[22] B. Goris, J. D. Beenhouwer, A. D. Backer, D. Zanaga, K. J. Batenburg, A. Sánchez-Iglesias, L. M. Liz-Marzán, S. V. Aert, S. Bals, J. Sijbers, G. V. Tendeloo, *Nano Lett.* **2015**, *15*, 6996.
[23] M. Escudero-Escribano, P. Malacrida, M. H. Hansen, U. G. Vej-Hansen, A. Velázquez-Palenzuela, V. Tripkovic, J. Schiøtz, J. Rossmeisl, I. E. L. Stephens, I. Chorkendorff, *Science* **2016**, *352*, 73.
[24] Y. Wang, J. Xiao, H. Zhu, Y. Li, Y. Alsaid, K. Y. Fong, Y. Zhou, S. Wang, W. Shi, Y. Wang, A. Zettl, E. J. Reed, X. Zhang, *Nature* **2017**, *550*, 487.
[25] S. J. Wang, H. Wang, K. Du, W. Zhang, M. L. Sui, S. X. Mao, *Nat. Commun.* **2014**, *5*, 3433.
[26] H. Zhu, J. Zhang, R. Yanzhang, M. Du, Q. Wang, G. Gao, J. Wu, G. Wu, M. Zhang, B. Liu, J. Yao, X. Zhang, *Adv. Mater.* **2015**, *27*, 4752.
[27] X. Zheng, J. Xu, K. Yan, H. Wang, Z. Wang, S. Yang, *Chem. Mater.* **2014**, *26*, 2344.
[28] Q. Lu, Y. Yu, Q. Ma, B. Chen, H. Zhang, *Adv. Mater.* **2016**, *28*, 1917.
[29] Y. Yin, Y. Zhang, T. Gao, T. Yao, X. Zhang, J. Han, X. Wang, Z. Zhang, P. Xu, P. Zhang, X. Cao, B. Song, S. Jin, *Adv. Mater.* **2017**, *29*, 1700311.
[30] W. F. Chen, K. Sasaki, C. Ma, A. I. Frenkel, N. Marinkovic, J. T. Muckerman, Y. Zhu, R. R. Adzic, *Angew. Chem., Int. Ed.* **2012**, *51*, 6131.
[31] M. Chatti, T. Gengenbach, R. King, L. Spiccia, A. N. Simonov, *Chem. Mater.* **2017**, *29*, 3092.
[32] Q. Ding, B. Song, P. Xu, S. Jin, *Chem* **2016**, *1*, 699.
[33] J. Kibsgaard, T. F. Jaramillo, F. Besenbacher, *Nat. Chem.* **2014**, *6*, 248.
[34] G. Henkelman, B. P. Uberuaga, H. A. Jónsson, *J. Chem. Phys.* **2000**, *113*, 9901.
[35] G. Kresse, J. Furthmüller, *Comput. Mater. Sci.* **1996**, *6*, 15.
[36] G. Kresse, J. Furthmüller, *Phys. Rev. B* **1996**, *54*, 11169.
[37] X. Hai, K. Chang, H. Pang, M. Li, P. Li, H. Liu, L. Shi, J. Ye, *J. Am. Chem. Soc.* **2016**, *138*, 14962.
[38] T. F. Jaramillo, K. P. Jorgensen, J. Bonde, J. H. Nielsen, S. Horch, I. Chorkendorff, *Science* **2007**, *317*, 100.
[39] Q. Liu, Q. Fang, W. Chu, Y. Wan, X. Li, W. Xu, M. Habib, S. Tao, Y. Zhou, D. Liu, T. Xiang, A. Khalil, X. Wu, M. Chhowalla, P. M Ajayan, L. Song, *Chem. Mater.* **2017**, *29*, 4738.
[40] H. Eyring, *J. Chem. Phys.* **1935**, *3*, 107.
[41] H. Eyring, *J. Chem. Phys.* **1936**, *4*, 283.
[42] H. Zhu, M. L. Du, M. Zhang, M. L. Zou, T. T. Yang, S. L. Wang, J. M. Yao, B. C. Guo, *Chem. Commun.* **2014**, *50*, 15435.